ADVANCED MATERIALS
www.advmat.de

Vertically Phase Separated Photomultiplication Organic Photodetectors with *p-n* Heterojunction Type Ultrafast Dynamic Characteristics

Myeong In Kim, Soonyong Lee, Jinhyeon Kang, Jaehyeong Kim, Ziang Wu, Jong Ho Won, Seyeon Baek, Dae Sung Chung, Jin Young Kim, In Hwan Jung, and Han Young Woo**

Photomultiplication (PM)-type organic photodetectors (OPDs), which typically form a homogeneous distribution (HD) of *n*-type dopants in a *p*-type polymer host (HD PM-type OPDs), have achieved a breakthrough in device responsivity by surpassing a theoretical limit of external quantum efficiency (EQE). However, they face limitations in higher dark current and slower dynamic characteristics compared to *p-n* heterojunction (*p-n* HJ) OPDs due to inherent long lifetime of trapped electrons. To overcome this, a new PM-type OPD is developed that demonstrates ultrafast dynamic properties through a vertical phase separation (VPS) strategy between the *p*-type polymer and *n*-type acceptor, referred to as VPS PM-type OPDs. Notably, VPS PM-type OPDs show three orders of magnitude increase in −3 dB cut-off frequency (120 kHz) and over a 200-fold faster response time (rising time = 4.8 µs, falling time = 8.3 µs) compared to HD PM-type OPDs, while maintaining high EQE of 1121% and specific detectivity of 2.53×10^{13} Jones at −10 V. The VPS PM-type OPD represents a groundbreaking advancement by demonstrating the coexistence of *p-n* HJ and PM modes within a single photoactive layer for the first time. This innovative approach holds the potential to enhance both static and dynamic properties of OPDs.

1. Introduction

Organic photodetectors (OPDs) are devices designed to detect and convert light into electrical signals utilizing organic semiconducting materials. These materials typically consist of sp^2 carbon-based conjugated polymers or small molecules distinguishing them from silicon-based photodetectors. OPDs find diverse applications, such as image sensors, medical imaging, environmental monitoring, and biometric security.[1] Particularly, they have gained considerable attention for their potential applications in flexible and wearable devices.[2] The organic OPD materials offer unique advantages including solution processibility, strong light absorption capabilities, and facile tunability of optical and electronic properties.[3] However, the intrinsic challenge in conjugated organic materials, characterized by a strong exciton binding energy, has driven the development of *p-n* heterojunction (*p-n* HJ) OPDs with a blended composition of *p*-type donors and *n*-type acceptors in comparable amounts.[4] This approach aims to enhance the separation of photo-induced excitons and facilitate the efficient transport of separated holes and electrons within the photoactive layer. The *p-n* HJ structure offers several benefits, such as low dark current density (J_d) and fast signal response. However, it faces challenges in achieving the

M. I. Kim, I. H. Jung
Department of Organic and Nano Engineering
and Human-Tech Convergence Program
Hanyang University
222 Wangsimni-ro, Seongdong-gu, Seoul 04763, Republic of Korea
E-mail: inhjung@hanyang.ac.kr

S. Lee, Z. Wu, H. Y. Woo
Department of Chemistry
Korea University
Seoul 02841, Republic of Korea
E-mail: hywoo@korea.ac.kr

J. Kang
Light/Display Convergence R&BD Division
Cheorwon Plasma Research Institute
7194 Geumgang-ro, Seo-myeon, Cheorwon-gun, Gangwon-do 24062,
Republic of Korea

J. Kim, J. Y. Kim
School of Energy and Chemical Engineering
Ulsan National Institute of Science and Technology (UNIST)
Ulsan 44919, Republic of Korea

J. H. Won
Department of Energy Engineering
Dankook University
Cheonan 31116, Republic of Korea

S. Baek, D. S. Chung
Department of Chemical Engineering
Pohang University of Science and Technology (POSTECH)
Pohang 37673, Republic of Korea

J. Y. Kim
Graduate School of Carbon Neutrality
Ulsan National Institute of Science and Technology (UNIST)
Ulsan 44919, Republic of Korea

The ORCID identification number(s) for the author(s) of this article can be found under https://doi.org/10.1002/adma.202404597

DOI: 10.1002/adma.202404597

theoretically limited external quantum efficiency (EQE) of 100%.[5] A recent breakthrough in OPD technology has manifested in the development of photomultiplication (PM)-type devices. In PM-type OPDs, the PM layer is predominantly composed of *p*-type polymer host, with only a minor fraction (≈1 wt%) of n-type dopants, forming homogenous distribution (HD) of *n*-type dopants in a p-type polymer host (HD PM-type OPDs).[6] When light irradiates the OPDs, excited electrons are captured by the distributed electron acceptors. Subsequently, holes migrate to the anode under reverse bias, establishing a percolation pathway for hole transport. Additional holes are then injected from cathode to achieve charge neutralization of trapped electrons in the PM layer. This configuration enables a larger number of holes to pass through the PM layer, while electrons remain captured by the electron acceptors. Consequently, a higher negative bias and longer excited electron lifetime result in greater photocurrent density (J_{ph}).[7] Remarkably, EQEs exceeding 2 210 000% have been reported at specific bias voltages when strong electron-withdrawing electron acceptors are employed.[8] However, it is important to note that typical HD PM-type OPDs exhibit much poorer dynamic characteristics and higher J_d values compared to *p-n* HJ-type OPDs due to the long lifetime of excited electrons inherent to this configuration (Table S1, Supporting Information).[9]

The performance of *p-n* HJ- and HD PM-type OPDs appears to exhibit a trade-off relationship.[9a,10] While *p-n* HJ-type OPDs demonstrate favorable dynamic characteristics, they suffer from limited static characteristics. Conversely, HD PM-type OPDs excel in static characteristics but fall short in dynamic performance. Ideally, achieving a PM-type OPD with low J_d and a fast signal response akin to *p-n* HJ-type OPDs while maintaining their unique high EQEs should represent a significant breakthrough in OPD technology.

In this study, we successfully demonstrated a new PM-type OPD that enables both superior dynamic and static performance by utilizing vertical phase separation (VPS) strategy between *p*-type polymer host and *n*-type acceptor dopant (VPS PM-type OPDs). To realize VPS in a photoactive layer, a polar diethylene glycol (DEG)-substituted nonfullerene acceptor (NFA), 2,2′-((2Z,2′Z)-((4,4,9,9-tetrakis(2-(2-(2-methoxyethoxy)ethoxy)ethyl)−4,9-dihydro-s-indaceno[1,2-b:5,6-b']dithiophene-2,7-diyl)bis(methaneylylidene))bis(3-oxo-2,3-dihydro-1H-indene-2,1-diylidene))dimalononitrile (IDIC-DEG), was synthesized and introduced as a dopant (1 wt%) into a hydrophobic *p*-type polymer poly(3-hexylthiophene-2,5-diyl) (P3HT) host. Due to the difference in surface energy between P3HT and IDIC-DEG, the small amount of hydrophilic IDIC-DEG dopants within a P3HT domain migrates toward the hydrophilic electron transporting layer (ETL). This migration of IDIC-DEG dopants results in a nonuniform distribution of acceptors in the active layer, forming pure P3HT domains as well as densely populated IDIC-DEG regions. This creates partial *p-n* heterojunction characteristics in the IDIC-DEG-crowded area. The VPS PM-type P3HT:IDIC-DEG (100:1, w/w) devices exhibited an EQE of 1121%, responsivity (R) of 4.81 A W^{-1} at −10 V, and significantly low J_d values of 8.88×10^{-8} A cm^{-2} (at −10 V, the lowest among reported PM-type devices), resulting in a specific detectivity (D^*) of 2.53×10^{13} Jones. Notably, our VPS PM-type P3HT:IDIC-DEG devices exhibited a remarkable increase in the −3 dB cut-off frequency (120 kHz) and over a 200-fold faster response time (rising time = 4.8 µs, falling time = 8.3 µs) compared to HD PM-type P3HT:2,2′-((2Z,2′Z)-((4,4,9,9-tetrahexyl-4,9-dihydro-*s*-indaceno[1,2-b:5,6-b′]dithiophene-2,7-diyl) bis(methanylylidene))bis(3-oxo-2,3-dihydro-1H-indene-2,1-diylidene))dimalononitrile (IDIC) (100:1, w/w) devices. To the best of our knowledge, our VPS PM-type OPD is the first report of the coexistence of *p-n* HJ and PM modes within a single photoactive layer. We believe that harnessing VPS within a PM layer represents a groundbreaking strategy capable of enhancing the dynamic properties of PM-type OPDs while maintaining high EQE and D^* values.

2. Results and Discussion

A representative NFA, IDIC was chosen as the control compound, and IDIC-DEG was engineered by incorporating hydrophilic oligoethylene glycol side chains onto the same conjugated framework of IDIC to induce spontaneous VPS within a P3HT domain. The unique morphological and electronic properties of IDIC-DEG were investigated and discussed through a comparative analysis with IDIC. P3HT was selected as the p-type material due to its well-established status as a donor polymer for PM-type OPDs. The IDIC-DEG was newly synthesized as shown in Scheme S1 (Supporting Information). Briefly, 2-(2-(2-methoxyethoxy)ethoxy)ethyl 4-methylbenzenesulfonate (DEG-Ts) was synthesized by tosylating triethylene glycol in dichloromethane (DCM). The indacenodithiophene (IDT) core was subsequently reacted with the DEG-Ts under basic conditions using potassium *tert*-butoxide to yield IDT-DEG. The product underwent a Vilsmeier–Haack reaction to form IDT-DEG-CHO in 40% yield. Finally, IDT-DEG-CHO was subjected to Knoevenagel condensation with 1-(dicyanomethylene)−3-indanone (INCN) to produce IDIC-DEG (yield 52%). Further details regarding the synthetic procedure of IDIC-DEG can be found in the Supporting Information. The molecular structures of the intermediates, IDIC-DEG, and IDIC were confirmed by ^{1}H and ^{13}C NMR spectroscopy and matrix-assisted laser desorption/ionization-time of flight (MALDI-TOF) mass spectrometry measurements, which showed a good agreement with the proposed structures (Figures S1–S9, Supporting Information). IDIC-DEG exhibited good solubility in common organic solvents such as chloroform (CF), DCM, chlorobenzene (CB), dimethyl formamide (DMF), ethyl acetate, acetone, and tetrahydrofuran.

Figure 1a,b shows the molecular structures and UV–vis absorption spectra of P3HT, IDIC, and IDIC-DEG in both solution (CF) and thin film states. In solution, the maximum absorption wavelength (λ_{max}) for P3HT, IDIC, and IDIC-DEG was 449, 668, and 651 nm, respectively. In the film states, these values shifted to 528, 705, and 707 nm, respectively. While P3HT exhibited strong absorption in the green light region, IDIC and IDIC-DEG demonstrated strong absorption in the red-NIR range. The optical bandgap (E_g^{opt}) of P3HT, IDIC, and IDIC-DEG was determined to be 1.91, 1.62, and 1.58 eV, respectively, from the absorption onset wavelength in the film state. While the optical properties of IDIC and IDIC-DEG were similar due to their identical conjugated backbone structures, IDIC-DEG exhibited a slightly smaller E_g^{opt} in the film state (despite a blueshifted absorption

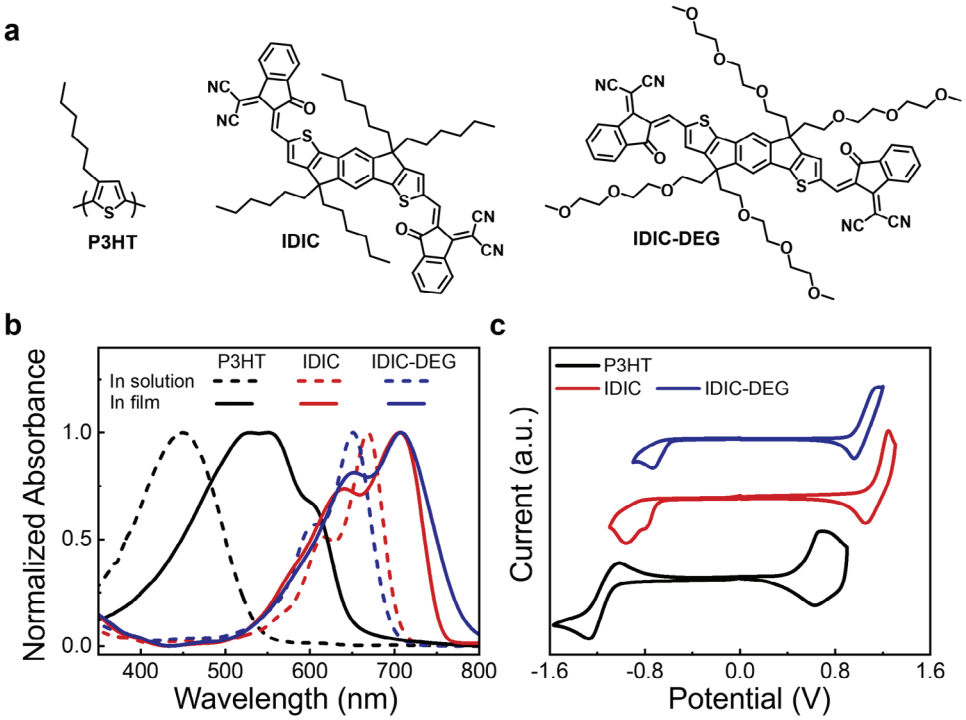

Figure 1. a) Molecular structures. b) UV–Vis absorption spectra, and (c) cyclic voltammograms of P3HT, IDIC, and IDIC-DEG.

compared to IDIC in solution), due to different intermolecular packing structures.

Cyclic voltammetry (CV) was conducted to determine the highest occupied molecular orbital (HOMO) and lowest unoccupied molecular orbital (LUMO) energy levels of donor and acceptor materials based on the oxidation and reduction onset potentials, respectively (Figure 1c). The HOMO energy levels of P3HT, IDIC, and IDIC-DEG were found to be −5.12, −5.75, and −5.57 eV, respectively, while their corresponding LUMO energy levels were −3.55, −3.92, and −4.03 eV, respectively. The higher HOMO and LUMO energy levels of P3HT indicate its *p*-type characteristics, while the significantly lower HOMO and LUMO energy levels of the synthesized NFAs confirm their *n*-type characteristics. When comparing the energy levels of the two NFAs, IDIC-DEG exhibited higher HOMO and lower LUMO energy levels than those of IDIC. The introduction of electron-donating DEG moieties into the IDT conjugated backbone enhanced the intramolecular charge transfer interaction between IDT and terminal electron-withdrawing moieties, leading to the lower electrochemical bandgap (E_g^{CV}). The optical and electrochemical properties of the photoactive materials are summarized in **Table 1**.

PM-type OPDs were constructed with an inverted-type architecture of indium tin oxide (ITO)/ETL/P3HT:NFA/MoO_x/Au. The vertical structure of devices was measured by cross-sectional scanning electron microscope (SEM) measurements (Figure S10, Supporting Information). The detailed device fabrication procedures can be found in the Experimental Section. In brief, polyethylenimineethoxylated (PEIE) was spin-cast on top of ITO as an ETL, and a mixture of P3HT and NFA (IDIC or IDIC-DEG, 100:1 w/w) in a CF:CB (8:2, v/v) cosolvent was deposited as a photoactive layer. Finally, 8 nm thick MoO_x and 100 nm thick Au layers were thermally deposited under a vacuum of 10^{-6} Torr, serving as the hole-transporting layer and top electrode, respectively.

First, the morphological properties of the PM photoactive layer with IDIC and IDIC-DEG NFAs were assessed by X-ray photoelectron spectroscopy (XPS) depth profile analysis. The samples were prepared with an architecture of ITO/PEIE/P3HT:NFA (10:1, w/w) and thermally annealed at 110 °C for 10 min. **Figure 2a–d** depicts the atomic depth profile as a function of etching time. Since the P3HT polymer donor does not contain nitrogen, the presence of nitrogen indicates the vertical distribution

Table 1. Optical and electrochemical properties of photoactive materials.

Material	$\lambda_{max,sol}$ [nm]	$\lambda_{max,film}$ [nm]	E_g^{opt} [eV][a)]	E_{HOMO} [eV][b)]	E_{LUMO} [eV][b)]	E_g^{CV} [eV][c)]
P3HT	449	528	1.91	−5.12	−3.55	1.57
IDIC	668	705	1.62	−5.75	−3.92	1.83
IDIC-DEG	651	707	1.58	−5.57	−4.03	1.54

[a)] Determined by 1240 nm/absorption edge (λ_{edge}) in film; [b)] Estimated from the onset of oxidation and reduction potential in CV measurements; [c)] Electrochemical bandgap.

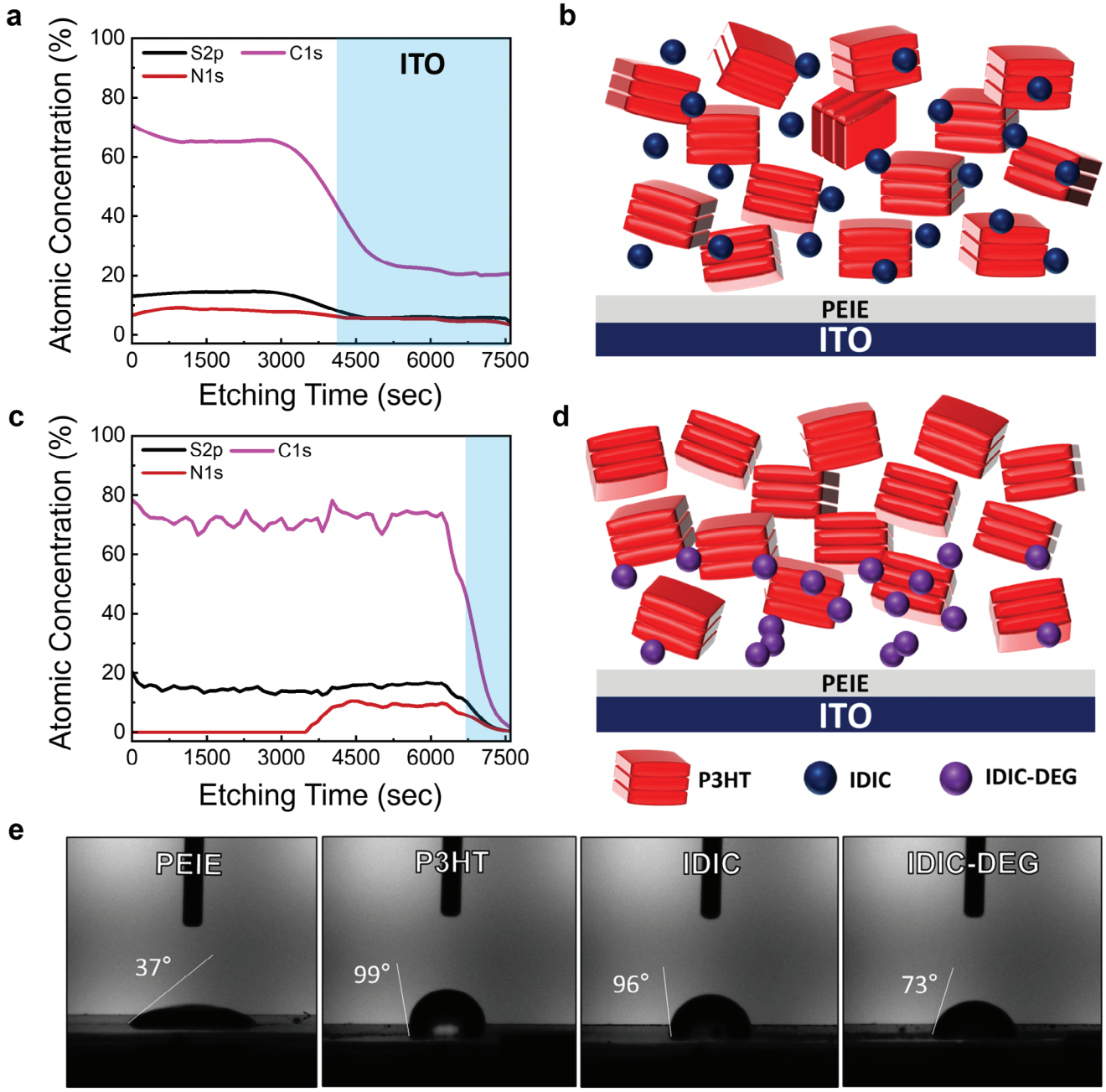

Figure 2. a,c) XPS depth profile and b,d) schematic illustration of photoactive layer for a,b) P3HT:IDIC and c,d) P3HT:IDIC-DEG blend films (10:1, w/w). e) Water contact angle measurements of PEIE, P3HT, IDIC, and IDIC-DEG films.

of NFAs (IDIC or IDIC-DEG). In the case of IDIC (Figure 2a), nitrogen is consistently detected during the etching process, suggesting that IDIC has a homogeneous distribution throughout the active layer. Conversely, in the case of IDIC-DEG (Figure 2c), nitrogen is absent until the etching time reaches 3500 s, after which it is continuously detected until the active layer is completely etched out. This implies that IDIC-DEG within the host P3HT has undergone vertical phase separation, positioning itself in close proximity to the ETL. The migration of IDIC-DEG toward the cathode layer, accompanied by partial aggregation, simultaneously leads to the formation of a pure P3HT domain, thereby partially creating a *p-n* HJ within a PM photoactive layer.

Second, cross-sectional scanning transmission electron microscopy-energy dispersive X-ray (STEM-EDX) analysis was conducted to evaluate the vertical distribution of NFAs (IDIC or IDIC-DEG) within the P3HT host. The samples were prepared in a similar manner for XPS depth profile analysis (Figure S11a, Supporting Information). Cross-sectional nitrogen mapping was carried out because nitrogen is only contained in NFAs. Due to the low concentration of NFAs and challenges in detecting

nitrogen due to its low fluorescence yield, the EDX line scan was carefully conducted along the indicated line near the PEIE/ITO interface (Figure S11b, Supporting Information). As shown in Figure S11c,d (Supporting Information), the nitrogen signal near the PEIE/ITO interface in the P3HT:IDIC-DEG films was clearly more intense than that in the P3HT:IDIC films. This indicates that IDIC-DEG is more concentrated near the PEIE/ITO interface, while IDIC is distributed throughout the active layer. This finding supports the presence of vertical phase separation in the P3HT:IDIC-DEG active layer, which is consistent with the XPS depth profile results (Figure 2a,c).

The morphological differences between IDIC-DEG and IDIC within the P3HT domain can be understood in terms of surface free energy and interfacial energy among PEIE, P3HT, IDIC, and IDIC-DEG, where PEIE serves as the electron-transporting material underneath the active layer. Surface free energies were calculated using Young's equation, and Owens and Wendt's geometric mean equation.[11] The wetting angles (θ) of the pristine films of PEIE, P3HT, IDIC, and IDIC-DEG were measured using water and ethanol droplets on the film surfaces by the sessile method (Figure 2e; and Figure S12, Supporting Information). The measured θ values of the PEIE, P3HT, IDIC, and IDIC-DEG pristine films were 14.4°, 36.6°, 21.0°, and 13.5°, respectively, for ethanol, and 36.5°, 98.9°, 95.9°, and 72.7°, respectively for water. The measured θ values are summarized in Table S2 (Supporting Information). From the wetting angle measurements, the total surface free energy (γ) and polarity were calculated, as shown in Table S3 (Supporting Information). The γ value of PEIE, P3HT, IDIC, and IDIC-DEG was 66.32, 18.87, 21.69, and 30.79 mJ m^{-2}, respectively, and the corresponding polarity was 0.90, 0.10, 0.09, and 0.56, respectively. P3HT and IDIC exhibited almost similar surface energy and polarity, suggesting good miscibility between them. In contrast, IDIC-DEG showed relatively high surface energy and polarity, indicating a better affinity toward the PEIE surface. As a result, the interfacial energy (γ_{ij}) between P3HT and IDIC was only 0.10 mJ m^{-2}, whereas that of between P3HT and IDIC-DEG showed significantly higher value of 7.81 mJ m^{-2}. This strongly supports the VPS behavior between P3HT and IDIC-DEG, where IDIC-DEG moves toward the ETL. As shown in Table S4 (Supporting Information), the γ_{ij} between PEIE and P3HT (or IDIC) is ≈43 mJ m^{-2}, whereas that between PEIE and IDIC-DEG is only 14 mJ m^{-2}. Thus, VPS occurs between P3HT and IDIC-DEG, whereas homogeneous mixing is more favorable between P3HT and IDIC. Moreover, as shown in Figure S13 (Supporting Information), the spin-coating process can enhance VPS formation because the active layer solution spreads out from the center. During spin-coating, IDIC-DEG exhibits a stronger affinity for the polar PEIE ETL layer and simultaneously moves toward the substrate. Additionally, the post-thermal annealing process of the active layer may further facilitate the migration of IDIC-DEG toward the ETL side. The surface roughness of the films was characterized using atomic force microscopy. As depicted in Figure S14 (Supporting Information), the root-mean-square roughness (R_q) of P3HT, P3HT:IDIC (100:1, w/w), and P3HT:IDIC-DEG (100:1, w/w) films was determined to be 13.7, 18.6, and 14.3 nm, respectively. Notably, the P3HT:IDIC blend films exhibited significantly rougher surfaces, likely attributed to the presence of rigid and planar IDIC molecules at the surface. Conversely, the comparable surface roughness observed in the P3HT and P3HT:IDIC-DEG films suggests that IDIC-DEG is preferentially located beneath the surface, likely facilitated by VPS.

The current density–voltage (J–V) curves for HD PM-type P3HT:IDIC and VPS PM-type P3HT:IDIC-DEG devices under negative bias conditions with 532 nm collimated LED light irradiation are presented in **Figure 3**. The device architecture is depicted along with the corresponding energy level diagram (Figure 3a,b). The R and D^* values were extracted at both −10 and −20 V.[12] First, the R value of the OPDs is defined as J_{ph} per incident light power (P_{light}), and it can be calculated using Equation (1):[13]

$$R = \frac{J_{ph}}{P_{light}} \quad \left(\text{A W}^{-1}\right) \tag{1}$$

Under light irradiation (0.1 mA cm^{-2}), the R values for HD PM-type P3HT:IDIC and VPS PM-type P3HT:IDIC-DEG devices were determined to be 8.49 and 4.81 A W^{-1}, respectively, at −10 V, and 20.2 and 15.0 A W^{-1}, respectively, at −20 V. When these R values are converted to EQE, the EQE values of HD PM-type P3HT:IDIC and VPS PM-type P3HT:IDIC-DEG devices reach to 1979% and 1121%, respectively, at −10 V and 4714% and 3494%, respectively, at −20 V. These data are well consistent with the measured EQE spectra (at −10 V) as a function of wavelength (Figure 3e). Such high EQE values exceeding 100% indicate the unique characteristics of PM-type OPDs. Second, the shot-noise-limited specific detectivity ($D_{sh}{}^*$) is one of the most crucial parameters for OPDs, as it is closely related to the "on/off ratio" of the devices. It can be calculated using the following Equation (2):

$$D_{sh}{}^* = \frac{R}{\sqrt{2qJ_d}} \quad \left(\text{cm Hz}^{0.5}\ \text{W}^{-1}\ \text{or Jones}\right) \tag{2}$$

where q represents the elementary charge and J_d is the dark current density. At −10 V, the J_d values for HD PM-type P3HT:IDIC and VPS PM-type P3HT:IDIC-DEG devices were measured to be 1.21×10^{-6} and 8.88×10^{-8} A cm^{-2}, respectively (Figure 3c,d). Consequently, the calculated $D_{sh}{}^*$ values were 1.36×10^{13} and 2.85×10^{13} Jones, respectively. The J_d value of 8.88×10^{-8} A cm^{-2} in the VPS PM-type P3HT:IDIC-DEG devices at −10 V was one of the lowest among reported PM-type devices. Although the R value of VPS PM-type P3HT:IDIC-DEG devices was lower than that of HD PM-type P3HT:IDIC devices, the VPS PM-type devices exhibited a noticeably higher $D_{sh}{}^*$ value due to the significant suppression of J_d compared to HD PM-type devices.

The noise current (i_n) of HD PM-type P3HT:IDIC and VPS PM-type P3HT:IDIC-DEG devices was also obtained to calculate D^* of OPDs. The i_n was extracted from the Fourier transform of the dark current. As shown in Figure 3f, the measured i_n values of HD PM-type P3HT:IDIC and VPS PM-type P3HT:IDIC-DEG devices were 2.25×10^{-13} and 5.70×10^{-14} A Hz$^{-0.5}$, respectively, at −10 V, and the corresponding D^* value was calculated from Equation (3) using the i_n, R, the area of the active layer (A) and the bandwidth (B):[14]

$$D^* = \frac{R\sqrt{AB}}{i_n} \quad \left(\text{cm Hz}^{0.5}\ \text{W}^{-1}\ \text{or Jones}\right) \tag{3}$$

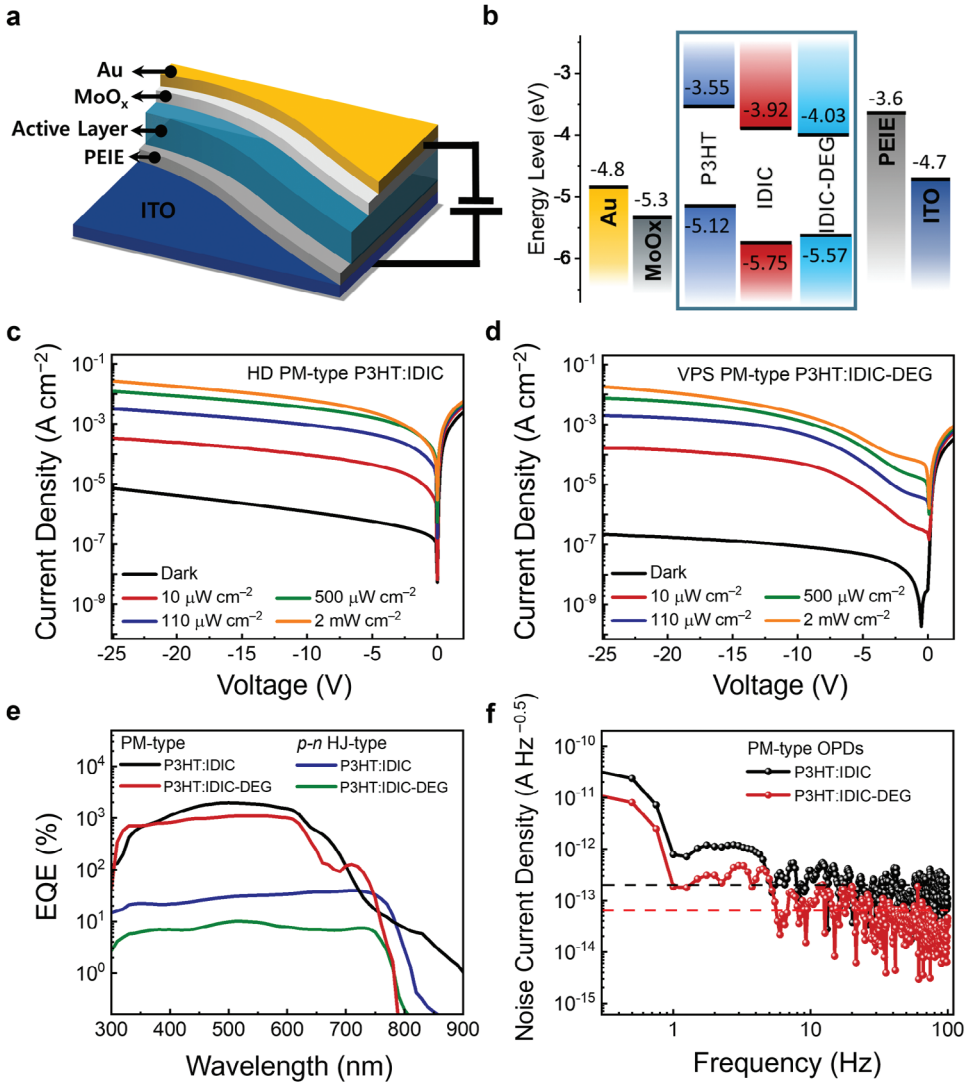

Figure 3. a) Device architecture and b) energy level diagram of PM OPDs. *J–V* curves of (c) P3HT:IDIC and (d) P3HT:IDIC-DEG based PM OPDs under 532 nm LED illumination by varying light intensity. e) EQE spectra of PM-type (at −10 V) and *p-n* HJ-type OPDs (at −2 V bias) as a function of wavelength. f) Noise current spectra of HD PM-type (P3HT:IDIC) and VPS PM-type (P3HT:IDIC-DEG) OPDs at −10 V.

The calculated D^* value of the HD PM-type P3HT:IDIC and VPS PM-type P3HT:IDIC-DEG devices was 1.13×10^{13} and 2.53×10^{13} cm $Hz^{0.5}$ W^{-1}, respectively, under light irradiation of 0.1 mA cm^{-2} at −10 V. The i_n value of VPS PM-type P3HT:IDIC-DEG devices was lower than that of HD PM P3HT:IDIC devices, and thus D^* values of VPS PM-type P3HT:IDIC-DEG devices were ≈2 times higher than those of HD PM-type P3HT:IDIC devices. This result is in a good agreement with the lower J_d and higher $D_{sh}{}^*$ values of VPS PM-type P3HT:IDIC-DEG devices. The summary of the device characteristics is further provided in Tables S5 and S6 (Supporting Information).

The detection limit of the OPDs was determined through the calculation of the noise equivalent power (NEP) value, which signifies the incident light power required to detect the photocurrent against the background dark current.[15] The calculated NEP values for the HD PM-type P3HT:IDIC and VPS PM-type P3HT:IDIC-DEG devices were 2.65×10^{-14} and 1.19×10^{-14} W $Hz^{-0.5}$, respectively, at −10 V. A significantly decreased NEP (by half) was obtained for the VPS PM-type P3HT:IDIC-DEG devices. The linear dynamic range (LDR) value was determined using Equation (4):

$$\text{LDR} = 20 \times \log \frac{J_{max}}{J_{min}} \text{ (dB)} \quad (4)$$

where J_{max} and J_{min} represent the maximum and minimum J_{ph} values, respectively, within the linear relationship between J_{ph} and P_{light}. The calculated LDR values at −10 V bias for HD PM-type P3HT:IDIC and VPS PM-type P3HT:IDIC-DEG devices were 74.3 and 87.0 dB, respectively, as shown in Figure S15 (Supporting Information). The improved LDR value in VPS PM-type P3HT:IDIC-DEG devices is attributed to their lower J_d characteristics, which lead to improved signal linearity at low light intensities.

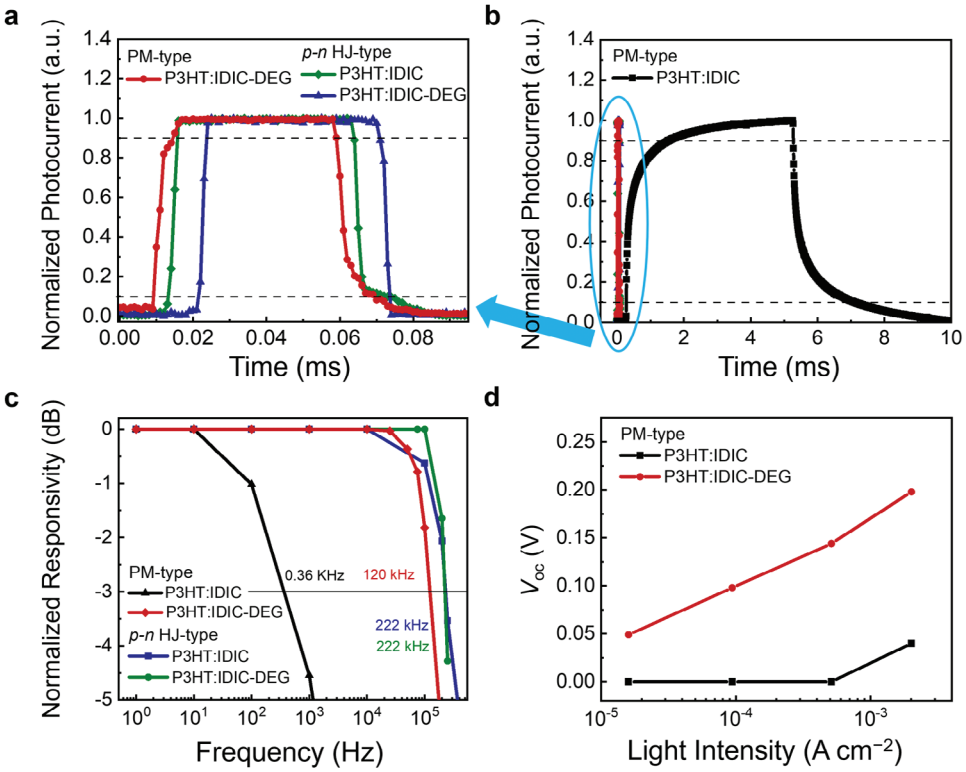

Figure 4. a) TPC spectral responses of (a) VPS PM-type P3HT:IDIC-DEG and *p-n* HJ-type OPDs and b) HD PM-type P3HT:IDIC devices. c) −3 dB cut-off frequency plots. d) Light intensity dependent V_{oc} measurements of P3HT:IDIC and P3HT:IDIC-DEG (100:1, w/w) films.

The dynamic characteristics of the PM-type OPDs were investigated through transient photocurrent (TPC) and the −3 dB cut-off frequency ($f_{-3\,dB}$) measurements of the devices under a light intensity of 1 mW cm^{-2} at −10 V (**Figure** 4a–c). The rising (t_r) and falling (t_f) response times of the TPC signals were defined as the times between the 10% and 90% points of the steady-state current.[16] The t_r for HD PM-type P3HT:IDIC and VPS PM-type P3HT:IDIC-DEG devices were 1300 and 4.8 µs, respectively, while the corresponding t_f values were 1800 and 8.3 µs, respectively. The response times of VPS PM-type P3HT:IDIC-DEG devices were ≈200 times faster than those of typical HD PM-type P3HT:IDIC devices. The $f_{-3\,dB}$ values were measured under 10 Hz modulated LED illumination. As shown in Figure 4c, the $f_{-3\,dB}$ values for HD PM-type P3HT:IDIC and VPS PM-type P3HT:IDIC-DEG devices were 0.36 and 120 kHz, respectively. The VPS PM-type P3HT:IDIC-DEG devices demonstrated a $f_{-3\,dB}$ value approximately three orders of magnitude higher than that of HD PM-type P3HT:IDIC devices. The summary of dynamic properties of P3HT:IDIC and P3HT:IDIC-DEG OPDs are provided in Table S7 (Supporting Information). Remarkably, to the best of our knowledge, these dynamic characteristics (t_r, t_f, and $f_{-3\,dB}$) of the VPS PM-type P3HT:IDIC-DEG devices are the best reported among PM-type OPDs. Table S1 (Supporting Information) summarizes the device performance of previously reported PM-type OPDs, and notably, our VPS PM-type devices exhibited distinguishably outstanding dynamic performance compared to all the references.

The ratio of P3HT:IDIC-DEG was varied from 100:1 to 5:1 w/w to optimize the PM characteristics in the devices. As shown in Figure S16 (Supporting Information), the static properties (*J–V* curve, EQE, and D_{sh}^{*}) significantly decreased as the acceptor ratio increased. This indicates that a ratio of approximately P3HT:IDIC-DEG = 100:1 w/w exhibits the most optimized OPD performance, and increasing the IDIC-DEG ratio in the P3HT host significantly decreases the PM characteristics of OPDs. In terms of dynamic properties, there were no significant changes depending on the acceptor ratio. However, the $f_{-3\,dB}$ characteristics were clearly enhanced as the acceptor ratio increased. With rapid dynamic characteristics being the major advantage of *p-n* HJ devices, the increased $f_{-3\,dB}$ values of PM-type P3HT:IDIC-DEG devices signify the strengthening of *p-n* HJ characteristics as the acceptor concentration increases.

Given the structural similarity between IDIC and IDIC-DEG and the inherent limitations in the dynamic properties of PM-type OPDs, the notable improvement of dynamic properties observed in the VPS PM-type P3HT:IDIC-DEG devices is of great interest. To comprehend the *p-n* HJ characteristics in VPS PM-type OPDs, we also fabricated typical *p-n* HJ-type devices (ITO/PEIE/active layer/MoO_x/Au) using P3HT:IDIC and P3HT:IDIC-DEG blend films (1:1.5, w/w). The *J–V* curves for both *p-n* HJ-type P3HT:IDIC and P3HT:IDIC-DEG devices are illustrated in Figure S17 (Supporting Information). The *R* values for *p-n* HJ-type P3HT:IDIC and P3HT:IDIC-DEG devices were 0.16 and 0.05 A W^{-1}, respectively, under light irradiation of 0.1 mA cm^{-2} at −2 V, corresponding to EQE values of 36% and 12%, respectively. The EQE values for both devices were less than 100%, following the typical characteristic behavior of *p-n* HJ photodiodes. The summary of the OPD characteristics is provided in

Table S8 (Supporting Information). The TPC and $f_{-3\,dB}$ of the *p-n* HJ-type OPDs were measured under the same conditions with the PM-type OPDs, under a light intensity of 1 mW cm^{-2} at −2 V. The t_r and t_f values for *p-n* HJ-type P3HT:IDIC devices were 2.4 and 5.2 µs, respectively, while those for *p-n* HJ-type P3HT:IDIC-DEG devices were 2.0 and 2.6 µs, respectively (Figure 4a). Additionally, the $f_{-3\,dB}$ values for both *p-n* HJ-type devices were measured to be 222 kHz (Figure 4c). Both *p-n* HJ-type devices exhibited ultrafast response times and frequency responses, providing a unique advantage of dynamic properties of *p-n* HJ-type OPDs.

Notably, for P3HT:IDIC devices, *p-n* HJ-type and HD PM-type OPDs demonstrated entirely different photo-detecting behaviors: *p-n* HJ-type OPDs exhibited low *R* values but fast dynamic characteristics, while PM-type OPDs exhibited the opposite behavior. This divergence is natural because *p-n* HJ-type and PM-type devices operate on distinct mechanisms.[9a,10] In *p-n* HJ-type OPDs, one pair of hole and electron is generated by absorbing one photon and the photo-induced holes and electrons transport to the anode and cathode. This characteristic leads to fast dynamic responses. Conversely, in PM-type OPDs, photo-induced electrons are trapped by the dispersed NFAs in the polymer host, allowing more than one hole to pass from the cathode to the anode under negative bias. This suggests that PM-type OPDs exhibit high EQE values exceeding 100% but have slower signal responses due to the lifetime of trapped electrons within the NFAs. However, in the case of P3HT:IDIC-DEG devices, the dynamic characteristics of PM-type devices resemble those of *p-n* HJ-type OPDs. The response times of VPS PM-type P3HT:IDIC-DEG devices (t_r = 4.8 µs and t_f = 8.3 µs) were comparable to those of *p-n* HJ-type P3HT:IDIC-DEG devices (t_r = 2.0 µs and t_f = 2.6 µs). The $f_{-3\,dB}$ value of VPS PM-type P3HT:IDIC-DEG devices (120 kHz) was also comparable to that of *p-n* HJ-type P3HT:IDIC-DEG devices (222 kHz). This strongly indicates that the VPS PM OPD structures also possess *p-n* HJ characteristics.

To provide more direct evidence of *p-n* HJ characteristics in VPS PM-type OPDs, we also investigated the V_{oc} versus incident light power (P_{in}) characteristics for HD PM-type P3HT:IDIC and VPS P3HT:IDIC-DEG devices. As shown in Figure 4d; and Figure S18 (Supporting Information), the V_{oc} of the HD PM-type P3HT:IDIC devices remained independent of P_{in}, showing a typical behavior of PM-type OPDs. In contrast, the V_{oc} of the VPS PM-type P3HT:IDIC-DEG devices gradually increased with increasing light intensity. The dependence of V_{oc} on light intensity implies that VPS PM-type P3HT:IDIC-DEG devices partially exhibit *p-n* HJ-type characteristics.[17] This VPS within a PM photoactive layer, resulting from the interfacial energy difference between P3HT and IDIC-DEG, simultaneously creates *p-n* HJ characteristics within the photoactive layer, which compensates for the limitations in dynamic responses of HD PM-type OPDs. The high J_d and slow signal response, previously identified as the main drawbacks of HD PM-type OPDs, have been significantly improved in the VPS PM-type OPDs. The introduction of polar DEG side chains to the NFA structure, leading to VPS within the PM photoactive layer, has paved the way for the development of new hybrid OPDs combining *p-n* HJ and PM OPDs.

The performance of VPS PM-type P3HT:IDIC-DEG OPDs clearly demonstrates the coexistence of *p-n* HJ and PM characteristics within the VPS PM layer. Although elucidating a definitive mechanism is currently challenging, we propose a plausible scenario illustrating how the presence of only 1% IDIC-DEG can induce *p-n* HJ characteristics within a PM layer via VPS, as depicted in **Figure 5**a,b. In regions densely populated with IDIC-DEG, the formation of continuous *n*-channels by some IDIC-DEG aggregates enables captured electrons to transport to the cathode, akin to charge transport in *p-n* HJ systems. The remaining isolated IDIC-DEGs may serve as electron traps during the PM process. Some studies have underscored the crucial role of electron trap density near the electrode in shaping the dynamic characteristics of PM-type OPDs.[6b,18] Enhanced trapping of electrons near cathode promotes hole tunneling injection under reverse bias. However, the response times—both rising and falling—reported in previous literatures (Table S1, Supporting Information) remain considerably slower compared to our findings. The VPS phenomenon delineated here differs from a mere elevation of electron trap density near the ETL in prior investigations. We anticipate that the establishment of *p-n* HJ characteristics proximal to the ETL will be pivotal in augmenting the dynamic characteristics of PM-type OPDs. This study presents, for the first time, the previously undocumented *p-n* HJ characteristics within a PM layer. While highlighting these significant findings, we acknowledge that the operational mechanisms remain open-ended questions, leaving ample room for further exploration into the operational principles.

3. Conclusions

We synthesized a new NFA, IDIC-DEG, featuring polar diethylene glycol side chains to enhance its polarity. IDIC-DEG shares an identical conjugated backbone with a representative IDIC NFA. The addition of DEG side chains rendered IDIC-DEG hydrophilic, resulting in a significant surface energy contrast with the control hydrophobic IDIC. PM-type OPDs were fabricated by constructing photoactive layers of P3HT:IDIC-DEG (100:1, w/w) and P3HT:IDIC (100:1, w/w). In the case of HD PM-type P3HT:IDIC devices, IDIC was evenly distributed within the P3HT host material, leading to the typical photodetecting properties observed in PM OPDs. However, in VPS PM-type P3HT:IDIC-DEG devices, a spontaneous vertical phase separation was observed between P3HT and IDIC-DEG due to their large interfacial energy difference. The IDIC-DEG dopants within the P3HT host concurrently migrated near the hydrophilic PEIE ETL. This simultaneous migration of IDIC-DEG in a photoactive layer resulted in pure P3HT domains as well as densely populated IDIC-DEGs, creating partial *p-n* HJ characteristics in the IDIC-DEG-enriched region. This unique VPS in a PM photoactive layer was confirmed by analyzing the XPS depth profile, and the existence of *p-n* HJ characteristics within a P3HT:IDIC-DEG PM layer was affirmed by measuring the light intensity dependent V_{oc}s in a photovoltaic mode. Owing to the coexistence of *p-n* HJ and PM characteristics in VPS PM-type P3HT:IDIC-DEG devices, they exhibited an approximately three orders of magnitude enhancement in −3 dB frequency, reaching 120 kHz, and a 200-fold faster response time (t_r = 4.8 µs, t_f = 8.3 µs) compared to HD PM-type P3HT:IDIC OPDs. To the best of our knowledge, these dynamic characteristics of the VPS PM-type P3HT:IDIC-DEG devices are the most superior among the reported PM-type OPDs. Harnessing VPS within a PM layer represents a groundbreaking strategy capable of enhancing the dynamic

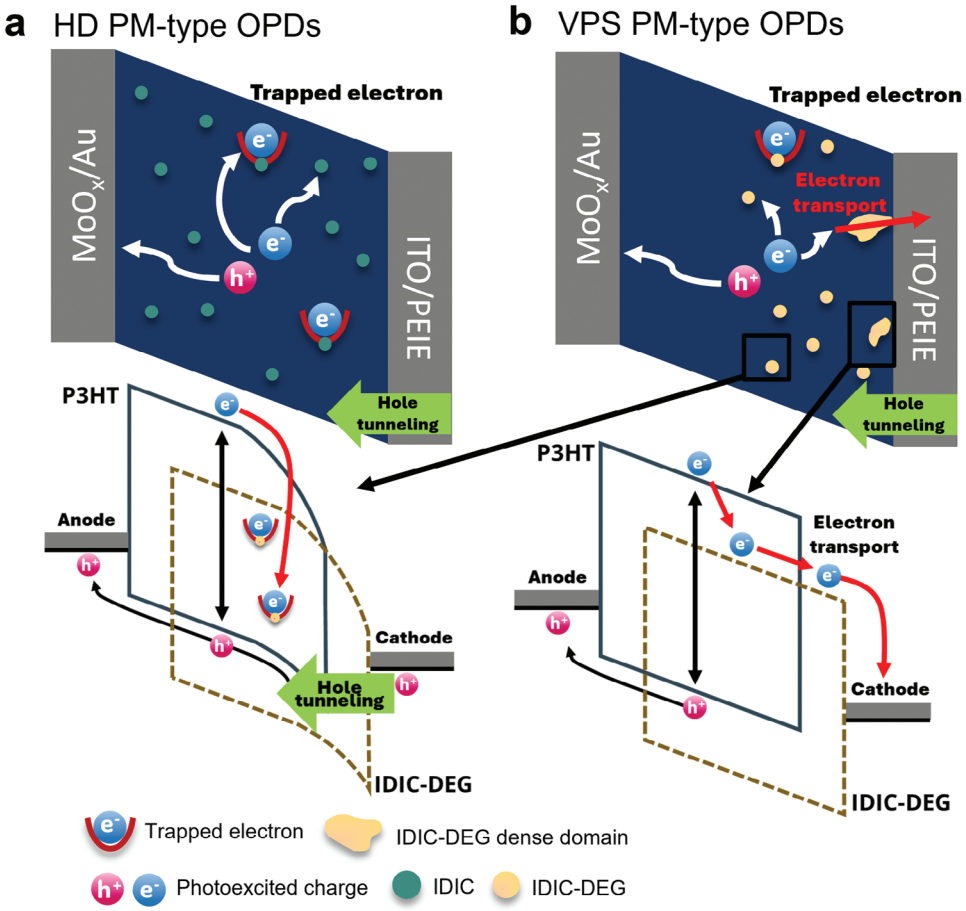

Figure 5. Suggested working mechanism of a) HD PM-type OPDs and b) VPS PM-type OPDs. Formation of *n*-channels in the regions densely populated with IDIC-DEG.

properties of PM-type OPDs while maintaining high EQE and D^* values.

4. Experimental Section

ITO-coated glasses, used as a transparent bottom electrode, underwent a cleaning process involving sonication with acetone, distilled water, and isopropyl alcohol for 20 min. A 0.1 wt% solution of PEIE dissolved in 2-methoxyethanol was spin-coated as an ETL at 3000 rpm for 30 s. Prior to the PEIE casting step, the cleaned ITO substrates underwent a 20 min UV-O_3 treatment. The PEIE-coated ITO substrates were thermally annealed at 150 °C for 10 min. These prepared substrates were transferred into an Ar-filled glove box. For the active layer, P3HT served as the host material, and IDIC and IDIC-DEG were used as electron acceptors. Two different-types of *p-n* HJ- and PM-type OPD devices were fabricated. To create the *p-n* HJ-type device, the weight ratio of P3HT to IDIC or IDIC-DEG was set at 1:1.5. These materials were dissolved in CF at a concentration of 25 mg mL^{-1}, with the addition of 1 vol% of 1,8-diiodooctane. After stirring for 2 h, the blend solution was spin-coated onto the PEIE-coated ITO substrate at 1000 rpm for 30 s and followed by thermal annealing at 110 °C for 10 min. In the case of the PM-type structure, the host P3HT donor and electron-trapping (IDIC or IDIC-DEG) acceptor ratio was set at 100:1 w/w. These materials were dissolved in a cosolvent system (CF:CB = 8:2, v/v) and stirred for 2 h at a concentration of 50 mg mL^{-1} based on the host material. The P3HT:NFA solution was spin-coated onto the PEIE-coated ITO substrate at 2000 rpm for 30 s and thermally annealed at 110 °C for 10 min. Finally, 8 nm thick MoO_x and 100 nm thick Au layers were thermally deposited under a vacuum of 10^{-6} Torr, serving as the hole transporting layer and top electrode, respectively. The active area of devices was 0.09 cm^2.

Supporting Information

Supporting Information is available from the Wiley Online Library or from the author.

Acknowledgements

M.I.K., S.L., and J.K. contributed equally to this work. This work was funded by National Research Foundation of Korea (NRF) (Nos. 2019R1A6A1A11044070, 2020M3H4A3081814, 2022M3H4A1A03067131, RS-2023-00304936, and 2023K2A9A2A06059546).

Conflict of Interest

The authors declare no conflict of interest.

Data Availability Statement

The data that support the findings of this study are available in the Supporting Information of this article.

Keywords

fast dynamic property, organic photodetector, photomultiplication, *p-n* heterojunction characteristic, vertical phase separation

Received: March 29, 2024
Revised: May 30, 2024
Published online: July 23, 2024

[1] a) Q. Lin, A. Armin, P. L. Burn, P. Meredith, *Nat. Photonics* **2015**, *9*, 687; b) T. Someya, Z. Bao, G. G. Malliaras, *Nature* **2016**, *540*, 379; c) Y. L. Wu, K. Fukuda, T. Yokota, T. Someya, *Adv. Mater.* **2019**, *31*, 1903687; d) G. Luo, J. Shi, W. Deng, Z. Chang, Z. Lu, Y. Zhang, R. Pan, J. Jie, X. Zhang, X. Zhang, *Adv. Mater.* **2023**, *35*, 2301020; e) H. Ren, J.-D. Chen, Y.-Q. Li, J.-X. Tang, *Adv. Sci.* **2021**, *8*, 2002418; f) Q. Liu, L. Li, J. Wu, Y. Wang, L. Yuan, Z. Jiang, J. Xiao, D. Gu, W. Li, H. Tai, Y. Jiang, *Nat. Commun.* **2023**, *14*, 6935; g) S. Y. Park, C. Labanti, R. A. Pacalaj, T. H. Lee, Y. Dong, Y.-C. Chin, J. Luke, G. Ryu, D. Minami, S. Yun, J.-I. Park, F. Fang, K.-B. Park, J. R. Durrant, J.-S. Kim, *Adv. Mater.* **2023**, *35*, 2306655; h) S. Lee, J. Lee, H. R. Sim, C. So, D. S. Chung, *Adv. Mater.* **2024**, *36*, 2310250; i) W. Jeong, J. Kang, D. Lee, C. Shin, H. Ahn, C. So, J. Ho Won, D. S. Chung, S. Cho, I. H. Jung, *Chem. Eng. J.* **2023**, *473*, 145178; j) J. Kim, H. Kweon, M. Lee, M. Kang, S. Lee, S. An, W. Lee, S. Choi, H. Choi, Y. Seong, H. Ham, H. Cha, J. Lim, D. H. Kim, B. Kim, D. S. Chung, *Adv. Mater.* **2023**, *35*, 2302786.

[2] a) H. Guo, S. Saifi, K. Fukuda, H.-M. Cheng, Z. Lou, X. Xu, *Digit. Signal Process.* **2022**, *125*, 103145; b) Z. Jiang, K. Yu, H. Wang, S. Rich, T. Yokota, K. Fukuda, T. Someya, *Adv. Mater. Technol.* **2021**, *6*, 2000956; c) B. C.-K. Tee, A. Chortos, A. Berndt, A. K. Nguyen, A. Tom, A. McGuire, Z. C. Lin, K. Tien, W.-G. Bae, H. Wang, P. Mei, H.-H. Chou, B. Cui, K. Deisseroth, T. N. Ng, Z. Bao, *Science* **2015**, *350*, 313; d) W. Gao, S. Emaminejad, H. Y. Y. Nyein, S. Challa, K. Chen, A. Peck, H. M. Fahad, H. Ota, H. Shiraki, D. Kiriya, D.-H. Lien, G. A. Brooks, R. W. Davis, A. Javey, *Nature* **2016**, *529*, 509; e) D. Kim, H.-J. Park, S.-H. Jung, W. J. Pyo, S. Z. Hassan, H. R. Sim, J.-H. Lee, D.-W. Jee, D. S. Chung, *Adv. Mater.* **2024**, *36*, 2309416; f) H. J. Cheon, T. K. An, Y.-H. Kim, *Macromol. Res.* **2022**, *30*, 71.

[3] a) P. C. Chow, T. Someya, *Adv. Mater.* **2020**, *32*, 1902045; b) J. Liu, M. Gao, J. Kim, Z. Zhou, D. S. Chung, H. Yin, L. Ye, *Mater. Today* **2021**, *51*, 475; c) H. Ren, J. D. Chen, Y. Q. Li, J. X. Tang, *Adv. Sci.* **2021**, *8*, 2002418; d) K. Xia, Y. Li, Y. Wang, L. Portilla, V. Pecunia, *Adv. Opt. Mater.* **2020**, *8*, 1902056; e) Z. Zhao, C. Xu, L. Niu, X. Zhang, F. Zhang, *Laser Photonics Rev.* **2020**, *14*, 2000262; f) K. Kranthiraja, H. Kim, J. Lee, U. K. Aryal, S. S. Reddy, R. D. Gayathri, T. Gokulnath, S.-H. Jin, *Macromol. Res.* **2023**, *31*, 897.

[4] a) T. H. Lee, Y. Dong, R. A. Pacalaj, S. Y. Park, W. Xu, J. S. Kim, J. R. Durrant, *Adv. Funct. Mater.* **2022**, *32*, 2208001; b) X. Zhao, T. Liu, H. Liu, S. Wang, X. Li, Y. Zhang, X. Hou, Z. Liu, W. Shi, T. J. S. Dennis, *ACS Appl. Mater. Interfaces* **2018**, *10*, 42715; c) D. Zhu, W. Jiang, Z. Ma, J. Feng, X. Zhan, C. Lu, J. Liu, J. Liu, Y. Hu, D. Wang, *Nat. Commun.* **2022**, *13*, 3454.

[5] a) C. Labanti, J. Wu, J. Shin, S. Limbu, S. Yun, F. Fang, S. Y. Park, C.-J. Heo, Y. Lim, T. Choi, *Nat. Commun.* **2022**, *13*, 3745; b) W. Jeong, J. Kang, S. Y. Lim, H. Ahn, H. M. Kim, J. H. Won, I. H. Jung, *Adv. Opt. Mater.* **2022**, *10*, 2102607; c) J. Huang, J. Lee, J. Vollbrecht, V. V. Brus, A. L. Dixon, D. X. Cao, Z. Zhu, Z. Du, H. Wang, K. Cho, *Adv. Mater.* **2020**, *32*, 1906027; d) P. Kafourou, Z. Qiao, M. Tóth, F. Aniés, F. Eisner, N. Gasparini, M. Heeney, *ACS Appl. Mater. Interfaces* **2022**, *14*, 39141.

[6] a) S. Xing, J. Kublitski, C. Hänisch, L. C. Winkler, T.-y. Li, H. Kleemann, J. Benduhn, K. Leo, *Adv. Sci.* **2022**, *9*, 2105113; b) S. Yoon, G. S. Lee, K. M. Sim, M. J. Kim, Y. H. Kim, D. S. Chung, *Adv. Funct. Mater.* **2021**, *31*, 2006448; c) H.-Y. Chen, M. K. F. Lo, G. Yang, H. G. Monbouquette, Y. Yang, *Nat. Nanotechnol.* **2008**, *3*, 543; d) J. Miao, F. Zhang, *Laser Photonics Rev.* **2019**, *13*, 1800204; e) S. Lee, G. S. Lee, M. Kang, Y. H. Ha, Y.-H. Kim, D. S. Chung, *Adv. Funct. Mater.* **2022**, *32*, 2204383.

[7] a) S. Lee, G. S. Lee, M. Kang, Y. H. Ha, Y. H. Kim, D. S. Chung, *Adv. Funct. Mater.* **2022**, *32*, 2204383; b) L. Li, F. Zhang, J. Wang, Q. An, Q. Sun, W. Wang, J. Zhang, F. Teng, *Sci. Rep.* **2015**, *5*, 9181; c) T. Park, S. Lee, M. Kang, S. H. Yu, G.-H. Nam, K. M. Sim, D. S. Chung, *Chem. Eng. J.* **2021**, *418*, 129354.

[8] J. Kim, M. Kang, S. Lee, C. So, D. S. Chung, *Adv. Mater.* **2021**, *33*, 2104689.

[9] a) S. G. Han, H. Lee, W. Choi, D. Lee, S. Kim, Y. Sung, S. Kim, K. Cho, *Adv. Funct. Mater.* **2021**, *31*, 2102087; b) J. Kublitski, *Organic Semiconductor Devices for Light Detection*, Springer, New York **2022**; c) L. Li, F. Zhang, W. Wang, Y. Fang, J. Huang, *Phys. Chem. Chem. Phys.* **2015**, *17*, 30712.

[10] a) L. Shi, Q. Liang, W. Wang, Y. Zhang, G. Li, T. Ji, Y. Hao, Y. Cui, *Nanomaterials* **2018**, *8*, 713; b) D. Yang, D. Ma, *Adv. Opt. Mater.* **2019**, *7*, 1800522.

[11] a) J. H. Won, S. C. Mun, G. H. Kim, H. M. Jeong, J. K. Kang, *Small* **2020**, *16*, 2001756; b) D. K. Owens, R. Wendt, *J. Appl. Polym. Sci.* **1969**, *13*, 1741.

[12] S. Xing, J. Kublitski, C. Hänisch, L. C. Winkler, T. y. Li, H. Kleemann, J. Benduhn, K. Leo, *Adv. Sci.* **2022**, *9*, 2105113.

[13] a) H. Kim, J. Kang, H. Ahn, I. H. Jung, *Dyes Pigm.* **2022**, *197*, 109910; b) H. Kim, J. Kang, M. I. Kim, W. Jeong, S. Baek, H. Ahn, D. S. Chung, I. H. Jung, *ACS Appl. Mater. Interfaces* **2023**, *15*, 57545.

[14] a) J. Huang, J. Lee, H. Nakayama, M. Schrock, D. X. Cao, K. Cho, G. C. Bazan, T.-Q. Nguyen, *ACS Nano* **2021**, *15*, 1753; b) J. Kublitski, A. Hofacker, B. K. Boroujeni, J. Benduhn, V. C. Nikolis, C. Kaiser, D. Spoltore, H. Kleemann, A. Fischer, F. Ellinger, *Nat. Commun.* **2021**, *12*, 551; c) Z. Wu, N. Li, N. Eedugurala, J. D. Azoulay, D.-S. Leem, T. N. Ng, *Npj Flex Electron.* **2020**, *4*, 6.

[15] a) C. Fuentes-Hernandez, W.-F. Chou, T. M. Khan, L. Diniz, J. Lukens, F. A. Larrain, V. A. Rodriguez-Toro, B. Kippelen, *Science* **2020**, *370*, 698; b) Y. Song, G. Yu, B. Xie, K. Zhang, F. Huang, *Appl. Phys. Lett.* **2020**, *117*, 093302.

[16] a) M. Y. Hadiyanto, R. Estrada, C.-C. Lee, S. Biring, A. K. Akbar, C.-Y. Li, C.-J. Shih, Y.-Z. Li, S.-W. Liu, *Org. Electron.* **2021**, *99*, 106356; b) R. Zhuo, Y. Wang, D. Wu, Z. Lou, Z. Shi, T. Xu, J. Xu, Y. Tian, X. Li, *J. Mater. Chem. C* **2018**, *6*, 299; c) H. Kim, J. Kang, J. Park, H. Ahn, I.-N. Kang, I. H. Jung, *Macromolecules* **2022**, *55*, 9489.

[17] J. Nolasco, A. Castro-Carranza, Y. León, C. Briones-Jurado, J. Gutowski, J. Parisi, E. von Hauff, *Sol. Energy* **2019**, *184*, 610.

[18] a) W. Wang, F. Zhang, M. Du, L. Li, M. Zhang, K. Wang, Y. Wang, B. Hu, Y. Fang, J. Huang, *Nano Lett.* **2017**, *17*, 1995. b) X. Zhao, M. Liu, K. Yang, Z. Zhao, J. Wang, Z. Zhou, X. Ma, F. Zhang, *Org. Electron.* **2022**, *108*, 106587.